LETTER

doi:10.1038/nature09786

The unusual minimum of sunspot cycle 23 caused by meridional plasma flow variations

Dibyendu Nandy[1], Andrés Muñoz-Jaramillo[2,3] & Petrus C. H. Martens[2,3]

Direct observations over the past four centuries[1] show that the number of sunspots observed on the Sun's surface varies periodically, going through successive maxima and minima. Following sunspot cycle 23, the Sun went into a prolonged minimum characterized by a very weak polar magnetic field[2,3] and an unusually large number of days without sunspots[4]. Sunspots are strongly magnetized regions[5] generated by a dynamo mechanism[6] that recreates the solar polar field mediated through plasma flows[7]. Here we report results from kinematic dynamo simulations which demonstrate that a fast meridional flow in the first half of a cycle, followed by a slower flow in the second half, reproduces both characteristics of the minimum of sunspot cycle 23. Our model predicts that, in general, very deep minima are associated with weak polar fields. Sunspots govern the solar radiative energy[8,9] and radio flux, and, in conjunction with the polar field, modulate the solar wind, the heliospheric open flux and, consequently, the cosmic ray flux at Earth[3,10,11].

The creation and emergence of tilted, bipolar sunspot pairs and their subsequent decay and dispersal through flux transport processes determine the properties of the solar magnetic cycle[6,12–17]. The average tilt angle of the sunspots of cycle 23 did not differ significantly from earlier cycles[2]. However, the axisymmetric meridional circulation of plasma[18]—which is observationally constrained only in the upper 10% of the Sun, where it has an average poleward speed of 20 m s^{-1}—is known to have significant intra- and intercycle variation[19–22]. The equatorward counterflow of this circulation in the solar interior is believed to have a crucial role; it governs the equatorward migration and spatiotemporal distribution of sunspots and determines the solar cycle period[6,22,23]. We perform kinematic solar dynamo simulations to investigate whether internal meridional flow variations can produce deep minima between cycles in general, and, in particular, explain the observed characteristics of the minimum of cycle 23 (Supplementary Information)—a comparatively weak dipolar field strength and an unusually long period without sunspots.

We use a recently developed axisymmetric, kinematic solar dynamo model[24] to solve the evolution equations for the toroidal and poloidal components of the magnetic field. This model has been further refined using a buoyancy algorithm that incorporates a realistic representation of bipolar sunspot eruptions following the double-ring formalism[25,26] and qualitatively captures the surface flux transport dynamics leading to solar polar field reversal[7] (including the observed evolution of the radial component of the Sun's dipolar field). To explore the effect of changing meridional flows on the nature of solar minima, it is necessary to introduce fluctuations in the meridional flow. The large-scale meridional circulation in the solar interior is believed to be driven by Reynolds stresses and small temperature differences between the solar equator and poles; variations in the flows may be induced by changes in the driving forces or through the feedback of magnetic fields[27]. The feedback is expected to be highest at the solar maximum (polar field minimum), when the toroidal magnetic field in the solar interior is the strongest. We therefore perform dynamo simulations by randomly varying the meridional flow speed between 15 and 30 m s^{-1} (with the same amplitude in both the hemispheres) at the solar cycle maximum, and study its effect on the nature of solar cycle minima. Details of the dynamo model are described in Supplementary Information.

Our simulations extend over 210 sunspot cycles corresponding to 1,860 solar years; for each of these simulated cycles, we record the meridional circulation speed, the cycle overlap (which includes the information on the number of days with no sunspots) and the strength of the polar radial field at cycle minimum. Figure 1 shows the sunspot butterfly diagram and surface radial field evolution over a selected 40-yr slice of the simulation. Here cycle to cycle variations (mediated by varying meridional flows) in the strength of the polar field at minimum and the structure of the sunspot butterfly diagram are apparent, hinting that the number of spotless days during a minimum is governed by the overlap (or lack thereof) of successive cycles.

We designate the minimum in activity following a given sunspot cycle, say n, as the minimum of n (because the sunspot eruptions from cycle n contribute to the nature of this minimum). We denote the amplitude of the meridional flow speed after the random change at

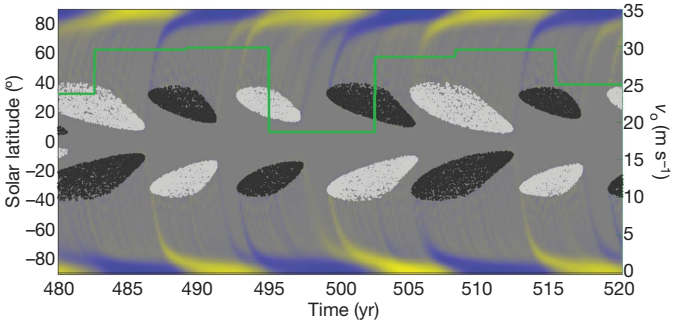

Figure 1 | Simulated sunspot butterfly diagram with a variable meridional flow. Starting with the pioneering telescopic observations of Galileo Galilei and Christopher Scheiner in the early seventeenth century, sunspots have been observed more or less continuously up to the present. Except for the period AD 1645–1715, known as the Maunder minimum, when hardly any sunspots were observed, the sunspot time series shows a cyclic variation going through successive epochs of maximum and minimum activity. This cyclic temporal variation in the latitude of sunspot emergence gives rise to the 'butterfly' diagram. In this simulated butterfly diagram, the green line shows the meridional flow speed, v_o, which is made to vary randomly between 15 and 30 m s^{-1} at sunspot maxima and to remain constant between maxima. The varying meridional flow induces cycle-to-cycle variations in both the amplitude as well as the distribution of the toroidal field in the solar interior from which bipolar sunspot pairs buoyantly erupt. This variation is reflected in the spatiotemporal distribution of sunspots, shown here as shaded regions (the lighter shade represents sunspots that have erupted from positive toroidal field and the darker shade represents those that have erupted from negative toroidal field). The sunspot butterfly diagram shows a varying degree of cycle overlap (of the 'wings' of successive cycles) at cycle minimum. The polar radial field strength (yellow, positive; blue, negative) is strongest at sunspot cycle minimum and varies significantly from one cycle minimum to another.

[1]Department of Physical Sciences, Indian Institute of Science Education and Research, Kolkata, Mohanpur 741252, West Bengal, India. [2]Department of Physics, Montana State University, Bozeman, Montana 59717, USA. [3]Harvard-Smithsonian Center for Astrophysics, Cambridge, Massachusetts 02138, USA.

the maximum of cycle n by v_n, which remains constant through the minimum of cycle n and changes again at the maximum of cycle $n+1$. According to this convention, the speed during the first (rising) half of cycle n would be v_{n-1}. To explore the relationship between the varying meridional flow, the polar field strength and cycle overlap, we generate statistical correlations between these quantities separately for the northern and southern solar hemispheres from our simulations over 210 sunspot cycles. We note that slight hemispheric asymmetries arise in the simulations owing to the stochastic nature of the active-region emergence process.

Unexpectedly, we find that there is no correlation between the flow speed at a given minimum (say v_n) and cycle overlap (or the number of spotless days) during that minimum, and the polar field strength at that minimum, B_r, is only moderately correlated with v_n (Fig. 2a, b). Because transport of magnetic flux by the meridional flow involves a finite time, it is likely that the characteristics of a given minimum could depend on the flow speed at an earlier time. We find that this is indeed the case (Fig. 2c, d), with cycle overlap (or the number of spotless days) and the polar field strength at a given minimum, n, being strongly correlated with the flow speed v_{n-1} (that is, meridional flow during the early, rising, part of cycle n). We also find that the cycle overlap is moderately correlated and that the polar field strength is strongly correlated with the change in flow speed between the first and second halves of the cycle (Fig. 2e, f). Taken together, these results show that a fast flow during the early part of the cycle, followed by a relatively slower flow during the later, declining, part of the cycle, results in a deep solar minimum.

The main characteristics of the minimum of solar cycle 23 are a large number of spotless days and a relatively weak polar field strength. In Fig. 3, we plot the polar field versus cycle overlap and find that very deep minima are in fact associated with relatively weak polar field strengths. Thus, the qualitative characteristics of the unusual minimum of sunspot cycle 23 are self-consistently explained in our simulations driven by changes in the Sun's meridional plasma flow. Our model predicts that, in general, extremely deep solar minima—with a large number of spotless days—would also be characterized by relatively weak solar polar field strengths.

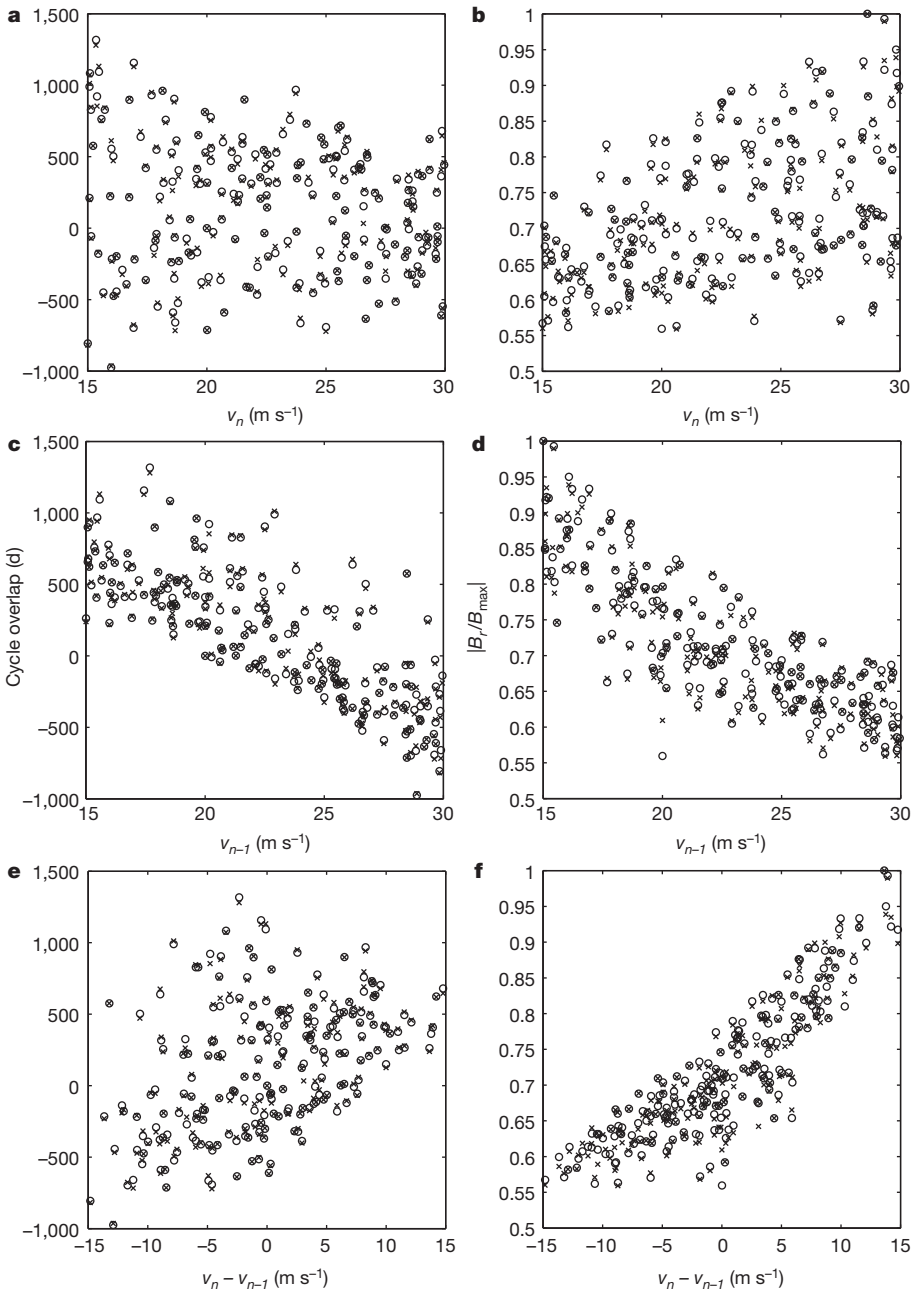

Figure 2 | Cycle overlap and polar field strength at solar minimum in response to variable meridional flows. Here v_n denotes flow speed during the minimum of sunspot cycle n, v_{n-1} denotes the speed during the early, rising, part of cycle n and $v_n - v_{n-1}$ denotes the change in flow speed between the declining and rising parts of the cycle. Cycle overlap is measured in days. Positive overlap denotes the number of days on which simulated sunspots from successive cycles erupted together, whereas negative overlap denotes the number of spotless days during a solar minimum; large negative overlap implies a deep (that is, long) minimum. The polar field ($|B_r/B_{max}|$) is represented by the peak radial field attained during a solar minimum normalized with respect to the maximum radial field attained during the complete model run (here $B_{max} = 16.66 \times 10^3$ G; see Supplementary Information for a discussion of polar field amplitudes). The relationship between the above parameters is determined by the Spearman's rank correlation coefficient (210 data points for each solar hemisphere, with northern- and southern-hemisphere data depicted as crosses and circles, respectively). **a**, Cycle overlap versus v_n; correlation coefficient: $r = -0.13$ (northern hemisphere), -0.13 (southern hemisphere); confidence level: $P = 93.42\%$ (northern hemisphere), 94.53% (southern hemisphere). **b**, Polar field strength versus v_n; $r = 0.45$, 0.45; $P = 99.99\%$, 99.99%. **c**, Cycle overlap versus v_{n-1}; $r = -0.81$, -0.80; $P = 99.99\%$, 99.99%. **d**, Polar field strength versus v_{n-1}; $r = -0.83$, -0.83; $P = 99.99\%$, 99.99%. **e**, Cycle overlap versus $v_n - v_{n-1}$; $r = 0.45$, 0.45; $P = 99.99\%$, 99.99%. **f**, Polar field strength versus $v_n - v_{n-1}$; $r = 0.87$, 0.87; $P = 99.99\%$, 99.99%. Evidently, a change from fast to slow internal meridional flow results in deep solar minima.

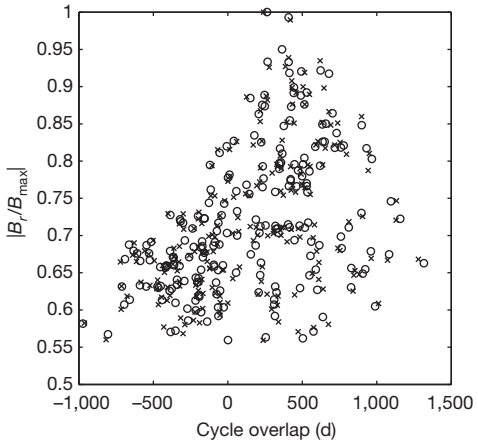

Figure 3 | Polar field strength versus cycle overlap at solar minimum. Simulated normalized polar field strength is plotted versus cycle overlap at sunspot cycle minimum. Spearman's rank correlation estimate: $r = 0.46$, 0.47 and $P = 99.99\%$, 99.99% for data from the northern (crosses) and southern (circles) hemispheres, respectively. The results show that a deep solar minimum with a large number of spotless days is typically associated with a relatively weak polar field—as observed during the minimum of sunspot cycle 23.

We find that our model results are robust with respect to reasonable changes in the driving parameters. Simulations with continuous flow variations (as opposed to discrete changes), relatively higher magnetic diffusivity and a different threshold for buoyant active-region eruption all yield qualitatively similar relationships between the nature of solar minima and flow speed variations (Supplementary Information).

Valuable insights into our simulation results may be gained by invoking the physics of meridional-flow-mediated magnetic flux transport. A faster flow (v_{n-1}) before and during the first half of cycle n would sweep the poloidal field of the previous cycle quickly through the region of differential rotation responsible for toroidal field induction; this would allow less time for toroidal field amplification and would hence result in a sunspot cycle (n) which is not too strong. The fast flow, followed by a slower flow during the second half of cycle n and persisting to the early part of the next cycle, would also distance the two successive cycles (that is, successive wings in the sunspot butterfly diagram), contributing to a higher number of spotless days during the intervening minimum. Moreover, a strong flow during the early half of cycle n would sweep both the positive and the negative polarity sunspots of cycle n (erupting at mid to high latitudes) to the polar regions; therefore, lower net flux would be available for cancelling the polar field of the old cycle and building the field of the new cycle—resulting in a relatively weak polar field strength at the minimum of cycle n. We believe that a combination of these effects contributes to the occurrence of deep minima such as that of solar cycle 23.

Independent efforts using surface flux transport simulations show that surface meridional flow variations alone (observed during solar cycle 23; see also Supplementary Information) are inadequate for reproducing the weak polar field of cycle 23 (ref. 28). Dynamo simulations—which encompass the entire solar convection zone—are therefore invaluable for probing the internal processes that govern the dynamics of the solar magnetic cycle, including the origin of deep minima such as that of cycle 23. We anticipate that NASA's recently launched Solar Dynamics Observatory will provide more precise constraints on the structure of the plasma flows deep in the solar interior, which could be useful for complementing these simulations.

Received 23 April 2010; accepted 5 January 2011.

1. Hoyt, D. V. & Schatten, K. H. Group sunspot numbers: a new solar activity reconstruction. *Sol. Phys.* **179,** 189–219 (1998).
2. Schrijver, C. J. & Liu, Y. The global solar magnetic field through a full sunspot cycle: observations and model results. *Sol. Phys.* **252,** 19–31 (2008).
3. Wang, Y.-M., Robbrecht, E. & Sheeley, N. R. Jr. On the weakening of the polar magnetic fields during solar cycle 23. *Astrophys. J.* **707,** 1372–1386 (2009).
4. Solar Influences Data Analysis Center. *Daily sunspot number* ⟨http://sidc.oma.be/sunspot-data/dailyssn.php⟩ (2011).
5. Solanki, S. K. Sunspots: an overview. *Astron. Astrophys. Rev.* **11,** 153–286 (2003).
6. Charbonneau, P. Dynamo models of the solar cycle. *Living Rev. Solar Phys.* **7,** 3 ⟨http://solarphysics.livingreviews.org/Articles/lrsp-2010-3/⟩ (2010).
7. Muñoz-Jaramillo, A., Nandy, D., Martens, P. C. H. & Yeates, A. R. A double-ring algorithm for modeling solar active regions: unifying kinematic dynamo models and surface flux-transport simulations. *Astrophys. J.* **720,** L20–L25 (2010).
8. Krivova, N. A., Balmaceda, L. & Solanki, S. K. Reconstruction of the solar total irradiance since 1700 from the surface magnetic flux. *Astron. Astrophys.* **467,** 335–346 (2007).
9. Lean, J. The Sun's variable radiation and its relevance for Earth. *Annu. Rev. Astron. Astrophys.* **35,** 33–67 (1997).
10. Solanki, S. K., Schüssler, M. & Fligge, M. Evolution of the Sun's large-scale magnetic field since the Maunder minimum. *Nature* **408,** 445–447 (2000).
11. Lara, A. *et al.* Coronal mass ejections and galactic cosmic-ray modulation. *Astrophys. J.* **625,** 441–450 (2005).
12. Babcock, H. W. The topology of the Sun's magnetic field and the 22-year cycle. *Astrophys. J.* **133,** 572–587 (1961).
13. Leighton, R. B. A magneto-kinematic model of the solar cycle. *Astrophys. J.* **156,** 1–26 (1969).
14. Choudhuri, A. R., Schussler, M. & Dikpati, M. The solar dynamo with meridional circulation. *Astron. Astrophys.* **303,** L29–L32 (1995).
15. Dikpati, M., de Toma, G. & Gilman, P. A. Predicting the strength of solar cycle 24 using a flux-transport dynamo-based tool. *Geophys. Res. Lett.* **33,** L05102 (2006).
16. Choudhuri, A. R., Chatterjee, P. & Jiang, J. Predicting solar cycle 24 with a solar dynamo model. *Phys. Rev. Lett.* **98,** 131103 (2007).
17. Yeates, A. R., Nandy, D. & Mackay, D. H. Exploring the physical basis of solar cycle predictions: flux transport dynamics and persistence of memory in advection-versus diffusion-dominated solar convection zones. *Astrophys. J.* **673,** 544–556 (2008).
18. Giles, P. M., Duvall, T. L., Scherrer, P. H. & Bogart, R. S. A subsurface flow of material from the Sun's equator to its poles. *Nature* **390,** 52–54 (1997).
19. Zhao, J. & Kosovichev, A. G. Torsional oscillation, meridional flows, and vorticity inferred in the upper convection zone of the Sun by time-distance helioseismology. *Astrophys. J.* **603,** 776–784 (2004).
20. González Hernández, I. *et al.* Meridional circulation variability from large-aperture ring-diagram analysis of global oscillation network group and Michelson Doppler imager data. *Astrophys. J.* **638,** 576–583 (2006).
21. Švanda, M., Kosovichev, A. G. & Zhao, J. Speed of meridional flows and magnetic flux transport on the Sun. *Astrophys. J.* **670,** L69–L72 (2007).
22. Hathaway, D. H., Nandy, D., Wilson, R. M. & Reichmann, E. J. Evidence that a deep meridional flow sets the sunspot cycle period. *Astrophys. J.* **589,** 665–670 (2003).
23. Nandy, D. & Choudhuri, A. R. Explaining the latitudinal distribution of sunspots with deep meridional flow. *Science* **296,** 1671–1673 (2002).
24. Muñoz-Jaramillo, A., Nandy, D. & Martens, P. C. H. Helioseismic data inclusion in solar dynamo models. *Astrophys. J.* **698,** 461–478 (2009).
25. Durney, B. R. On a Babcock-Leighton solar dynamo model with a deep-seated generating layer for the toroidal magnetic field. IV. *Astrophys. J.* **486,** 1065–1077 (1997).
26. Nandy, D. & Choudhuri, A. R. Toward a mean field formulation of the Babcock-Leighton type solar dynamo. I. α-coefficient versus Durney's double-ring approach. *Astrophys. J.* **551,** 576–585 (2001).
27. Rempel, M. Origin of solar torsional oscillations. *Astrophys. J.* **655,** 651–659 (2007).
28. Jiang, J., Işik, E., Cameron, R. H., Schmitt, D. & Schüssler, M. The effect of activity-related meridional flow modulation on the strength of the solar polar magnetic field. *Astrophys. J.* **717,** 597–602 (2010).

Supplementary Information is linked to the online version of the paper at www.nature.com/nature.

Acknowledgements This work was supported through the Ramanujan Fellowship of the Government of India at the Indian Institute of Science Education and Research, Kolkata, and by a NASA Living With a Star grant to the Smithsonian Astrophysical Observatory and Montana State University. We are grateful to D. Hathaway for providing the observational data on days without sunspots; the analysis of these data is reported in Supplementary Fig. 1.

Author Contributions D.N. conceived the principal idea and, in conjunction with P.C.H.M. and A.M.-J., planned the simulations, which were performed by A.M.J. under the guidance of D.N. and P.C.H.M. D.N. led the interpretation of the results and all authors contributed to writing the paper.

Author Information Reprints and permissions information is available at www.nature.com/reprints. The authors declare no competing financial interests. Readers are welcome to comment on the online version of this article at www.nature.com/nature. Correspondence and requests for materials should be addressed to D.N. (dnandi@iiserkol.ac.in).

Supplementary material for: The unusual minimum of sunspot cycle 23 caused by meridional plasma flow variations

Dibyendu Nandy[1], Andrés Muñoz-Jaramillo[2,3] & Petrus C. H. Martens[2,3]

[1]*Indian Institute for Science Education and Research, Kolkata, Mohampur 741252, West Bengal, India*

[2]*Department of Physics, Montana State University, Bozeman, MT 59717, USA*

[3]*Harvard-Smithsonian Center for Astrophysics, Cambridge, MA 02138, USA*

1 Characteristics of the Minimum of Solar Cycle 23

The solar magnetic cycle goes through periods of successive maxima and minima in activity which is manifested in a variation in the number of sunspots observed on the solar surface. The minimum of solar activity is often parameterized by the number of days without sunspots (i.e. spotless days). The recently concluded solar minimum following sunspot cycle 23 was unusually long, with the largest number of spotless days recorded in the space age (see Figure 1). Moreover, this minimum was also characterized by a relatively weak solar polar field strength as compared to the previous three cycles, for which direct polar field observations exists.

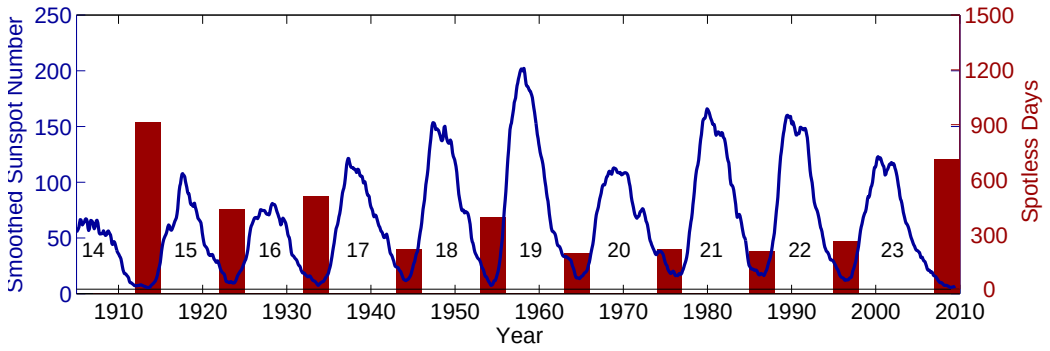

Figure 1: Sunspot cycles over the last century. The blue curve shows the cyclic variation in the number of sunspots (left-hand y-axis) with time (x-axis). The red bars shows the cumulative number of sunspot-less days (right-hand y-axis) between successive maximum; the minimum of sunspot cycle 23 was the longest in the space age with the largest number of spotless days. Nonetheless, the recorded sunspot history shows solar cycles 13 and 14 had even larger number of spotless days; hence, although the recently concluded minimum was unusual, it is not unique..

2 The Dynamo Model

In our simulation we solve the kinematic, axisymmetric dynamo equations:

$$\frac{\partial A}{\partial t} + \frac{1}{s}\left[\mathbf{v}_p \cdot \nabla(sA)\right] = \eta\left(\nabla^2 - \frac{1}{s^2}\right)A, \tag{1}$$

$$\frac{\partial B}{\partial t} + s\left[\mathbf{v}_p \cdot \nabla\left(\frac{B}{s}\right)\right] + (\nabla \cdot \mathbf{v}_p)B = \eta\left(\nabla^2 - \frac{1}{s^2}\right)B + s\left([\nabla \times (A\hat{\mathbf{e}}_\phi)] \cdot \nabla\Omega\right) + \frac{1}{s}\frac{\partial \eta}{\partial r}\frac{\partial (sB)}{\partial r}, \tag{2}$$

where A is the ϕ-component of the potential vector (from which B_r and B_θ can be obtained), B is the toroidal field (B_ϕ), v_p is the meridional flow, Ω the differential rotation, η the turbulent magnetic diffusivity and $s = r\sin(\theta)$. Conspicuous by its absence is the so-called poloidal source (traditionally known as the dynamo α-effect); in this work we introduce a more accurate treatment of the Babcock-Leighton[12,13] poloidal field regeneration algorithm as a discreet process composed of individual bipolar sunspot pairs (also known as Active Regions, ARs; more below). Kinematic dynamo models based on this Babcock-Leighton poloidal field regeneration mechanism have been successful in reproducing the large-scale properties of the solar cycle[6] and is strongly supported by recent observations[29]. We also need to define three more ingredients: meridional flow, differential rotation and turbulent magnetic diffusivity. We use appropriate choices for these physical ingredients which make our simulations relevant for the Sun; these are discussed in the ensuing sections. More details regarding kinematic dynamo models can be found in a review by Charbonneau[6] and references therein.

3 Modeling Individual Active Regions

It is currently believed that the recreation of poloidal field is caused primarily by the emergence of ARs, and their subsequent diffusion and transport towards the poles; an idea first introduced by Babcock[12] and further elaborated by Leighton[13]. Due to the crucial role of ARs, modeling their emergence accurately within the dynamo process is important. In order to do this, we follow an idea proposed by Durney[25] (and further elucidated by Nandy & Choudhuri[26]) of using ring duplets, although with an improved version which addresses the two main deficiencies of the earlier algo-

rithms: strong sensitivity to changes in grid resolution and the introduction of sharp discontinuities on the ϕ component of the potential vector A.

We define the ϕ component potential vector A corresponding to an AR as:

$$A_{ar}(r,\theta) = K_0 A(\Phi) F(r) G(\theta), \tag{3}$$

where $K_0 = 400$ is a constant we introduce to insure super-critical solutions and $A(\Phi)$ defines the strength of the ring-duplet and is determined by flux conservation. $F(r)$ is defined as

$$F(r) = \begin{cases} 0 & r < R_\odot - R_{ar} \\ \frac{1}{r}\sin^2\left[\frac{\pi}{2R_{ar}}(r - (R_\odot - R_{ar}))\right] & r \geq R_\odot - R_{ar} \end{cases}, \tag{4}$$

where $R_\odot = 6.96 \times 10^8$ m corresponds to the radius of the Sun and $R_{ar} = 0.15 R_\odot$ represents the penetration depth of the AR. Finally, $G(\theta)$ is easier to define in integral form and in the context of the geometry of the radial component of the magnetic field on the surface. In Figure 2-a we present a plot of the two super-imposed polarities of an AR after being projected on the r-θ plane. In order to properly describe such an AR we need to define the following quantities: the co-latitude of emergence θ_{ar}, the diameter of each polarity of the duplet Λ, for which we use a fixed value of 6^o (heliocentric degrees) and the latitudinal distance between the centers $\chi = \arcsin[\sin(\gamma)\sin(\Delta_{ar})]$, which in turn depends on the angular distance between polarity centers $\Delta_{ar} = 6^o$ and the AR tilt angle γ; χ is calculated using the spherical law of sines. In terms of these quantities, the latitudinal dependence for each polarity is determined by the following piecewise function (use the top signs

for the positive polarity and the lower for negative):

$$B_{\pm}(\theta) = \begin{cases} 0 & \theta < \theta_{ar} \mp \frac{\chi}{2} - \frac{\Lambda}{2} \\ \pm\frac{1}{\sin(\theta)}\left[1 + \cos\left(\frac{2\pi}{\Lambda}(\theta - \theta_{ar} \pm \frac{\chi}{2})\right)\right] & \theta_{ar} \mp \frac{\chi}{2} - \frac{\Lambda}{2} \leq \theta < \theta_{ar} \mp \frac{\chi}{2} + \frac{\Lambda}{2} \\ 0 & \theta \geq \theta_{ar} \mp \frac{\chi}{2} + \frac{\Lambda}{2} \end{cases} \quad (5)$$

In terms of these piecewise functions $G(\theta)$ becomes:

$$G(\theta) = \frac{1}{\sin\theta}\int_0^{\theta} [B_-(\theta') + B_+(\theta')]\sin(\theta')d\theta'. \quad (6)$$

A model AR is shown in Figure 2-b. This AR is located at a latitude of 40^o and has a penetration depth of $0.85R_\odot$. The depth of penetration of the AR is motivated from results indicating that the disconnection of an AR flux-tube happens deep down in the CZ[30].

4 Recreating the Poloidal Field

Given that the accumulated effect of all ARs is what regenerates the poloidal field, we need to specify an algorithm for AR eruption and decay in the context of the solar cycle. For each hemisphere independently and on each solar day of our simulation we perform the following procedure:

1. Search for magnetic fields exceeding than a buoyancy threshold $B_c = 5 \times 10^4$ Gauss on a specified layer at the bottom of the CZ ($r = 0.71R_\odot$), and record their latitudes.

2. Choose randomly one of the latitudes found on Step 1 and calculate the amount of magnetic flux present within it's associated toroidal ring. The probability distribution we use is not uniform, but is restricted to observed active latitudes. We do this by making the probability

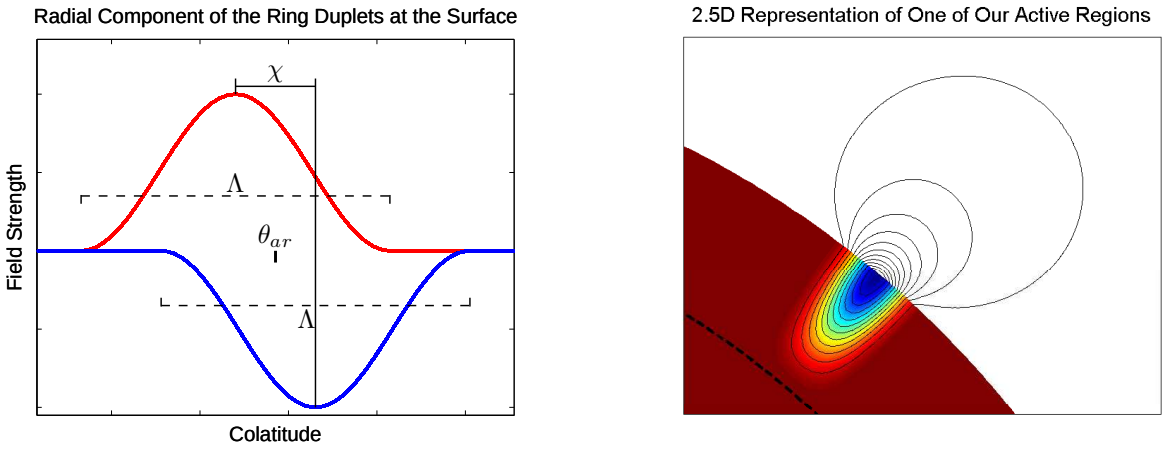

(a) (b)

Figure 2: (a) Superimposed magnetic field of the two polarities of a modeled active region (tilted bipolar sunspot pair). The different quantities involved are: the co-latitude of emergence θ_{ar}, the diameter of each polarity of the duplet Λ and the latitudinal distance between the centers χ. (b) Field lines of one of our model active regions including a potential field extrapolation for the region outside of the Sun. Contours correspond to field lines that trace the poloidal components and in this example their sense is counter-clockwise. The dashed line is included for reference and corresponds to a depth of $0.85R_{\odot}$.

function drop steadily to zero between 30^o (-30^o) and 40^o (-40^o) in the northern (southern) hemisphere:

$$P(\theta) \propto \left(1 + \mathrm{erf}\left[\frac{\theta - 0.305\pi}{0.055\pi}\right]\right)\left(1 - \mathrm{erf}\left[\frac{\theta - 0.694\pi}{0.055\pi}\right]\right). \quad (7)$$

3. Calculate the corresponding AR's tilt, using the local field strength B_0, the calculated flux Φ_0 and the latitude of emergence λ. For this we use the expression found by Fan, Fisher &

McClymont[31] ($\gamma \propto \Phi_0^{1/4} B_0^{-5/4} \sin(\lambda)$).

4. Reduce the magnetic field of the toroidal ring from which the AR originates. In order to do this, we first estimate how much magnetic energy is present on a partial toroidal ring (after removing a chunk with the same angular size as the emerging AR). Given that this energy is smaller than the one calculated with a full ring, we set the value of the toroidal field such that the energy of a full toroidal ring filled with the new magnetic field strength is the same as the one calculated with the old magnitude for a partial ring.

5. Deposit an AR (as defined in Section 3), at the same latitude chosen on Step 2, whose strength is determined by the flux calculated in Step 2 and whose tilt was calculated on Step 3.

5 Meridional Flow

We use the meridional profile of Muñoz-Jaramillo, Nandy and Martens[24] (MNM09), which closely represents the observed features present in helioseismic meridional flow data and is defined by the following stream funcion:

$$\Psi(r,\theta) = \frac{v_0(t)}{r}(r - R_p)(r - R_\odot) \sin\left(\pi \frac{r - R_p}{R_1 - R_p}\right)^a \sin^{(q+1)}(\theta)\cos(\theta), \tag{8}$$

where $q = 1$ governs the latitudinal dependence, $R_p = 0.675 R_\odot$ the penetration depth, $a = 1.92$ and $R_1 = 1.029 R_\odot$ govern the location of the peak of the poleward flow and the amplitude and location of the equatorward return flow. For more details please refer to MNM09[24]. In order to test the impact of a changing meridional flow on the solar cycle, $v_0(t)$ is set such that the peak

amplitude of the meridional flow at the surface varies between $15-30$m/s. We track the polar field amplitude and produce random changes in $v_0(t)$ at sunspot maximum.

6 Differential Rotation

We use the analytical form of Charbonneau et al.[32]. It is defined as:

$$\Omega_A(r,\theta) = 2\pi\left[\Omega_c + \tfrac{1}{2}\left(1+\texttt{erf}\left(\tfrac{r-r_{tc}}{w_{tc}}\right)\right)(\Omega_e-\Omega_c+(\Omega_p-\Omega_e)\Omega_S(\theta))\right]$$
$$\Omega_S(\theta) = a\cos^2(\theta)+(1-a)\cos^4(\theta), \tag{9}$$

where $\Omega_c = 432$ nHz is the rotation frequency of the core, $\Omega_e = 470$ nHz is the rotation frequency of the equator, $\Omega_p = 330$ nHz is the rotation frequency of the pole, $a = 0.483$ is the strength of the $\cos^2(\theta)$ term relative to the $\cos^4(\theta)$ term, $r_{tc} = 0.7R_\odot$ the location of the tachocline and $w_{tc} = 0.025R_\odot$ half of its thickness.

7 Turbulent Magnetic Diffusivity

The final ingredient of this model is a radially dependent magnetic diffusivity; in this work we use a double-step profile given by

$$\eta(r) = \eta_{bcd} + \frac{\eta_{cz}-\eta_{bcd}}{2}\left(1+\text{erf}\left(\frac{r-r_{cz}}{d_{cz}}\right)\right) + \frac{\eta_{sg}-\eta_{cz}-\eta_{bcd}}{2}\left(1+\text{erf}\left(\frac{r-r_{sg}}{d_{sg}},\right)\right) \tag{10}$$

where $\eta_{bcd} = 10^8$ cm^2/s corresponds to the diffusivity at the bottom of the computational domain, $\eta_{cz} = 10^{11}$ cm^2/s corresponds to the diffusivity in the convection zone, $\eta_{sg} = 10^{12}$ cm^2/s corresponds to the near-surface supergranular diffusivity and $r_{cz} = 0.71R_\odot$, $d_{cz} = 0.015R_\odot$,

$r_{sg} = 0.95R_\odot$ and $d_{sg} = 0.025R_\odot$ characterize the transitions from one value of diffusivity to the other.

8 Numerical Methods

In order to solve the 2.5 dynamo equations (Eq. 1 & 2) we transform our system of Partial Differential Equations(PDEs) to a system of coupled Ordinary Differential Equations(ODEs) by discretizing the spatial operators using finite differences. For advective terms we use a third order upwind scheme, for diffusive terms we use a second order space centered scheme and for other first derivative terms we use a second order space centered scheme. We then use an exponential propagation method to integrate the equations in time[24,33,34].

Our computational domain comprises the entire solar convection zone and a small section of the top radiative region ($0.55R_\odot \leq r \leq R_\odot$ and $0 \leq \theta \leq \pi$). We use a 300×500 uniformly spaced grid in radius (300 points) and colatitude (500 points). Our boundary conditions are:

$$\begin{aligned} &A(r, \theta = 0) = 0, \quad \tfrac{\partial (rA)}{\partial r}|_{r=R_\odot} = 0, \quad A(r, \theta = \pi) = 0, \quad A(r = 0.55R_\odot, \theta) = 0 \\ &B(r, \theta = 0) = 0, \quad B(r = R_\odot, \theta) = 0, \quad B(r, \theta = \pi) = 0, \quad \tfrac{\partial (rB)}{\partial r}|_{r=0.55R_\odot} = 0, \end{aligned} \tag{11}$$

which correspond to a conductive core at $r = 0.55R_\odot$, a perfect vacuum at $r = R_\odot$ and the rotation axis in an axisymmetric formulation at $\theta = 0, \pi$.

9 Sensitivity to Changes in the Simulation Setup

The representative simulation results presented earlier (which we term as the reference solution) were performed with the parameters and model setup as described in previous sections. Our realistic method of handling solar active regions is a major improvement within the framework of solar dynamo models and has been demonstrated to capture accurately the observed surface flux transport dynamics leading to polar field reversal[7]. The internal meridional flow profile that we have used is based on the best available constraints from helioseismic data[20,24] and the standard model of the solar interior[35]. In our simulations we have used a peak speed randomly varying between a reasonable range while keeping the internal profile unchanged and as constrained in MNM09[24]. This variation is assumed to be instantaneous in our reference simulations. The internal diffusivity profile in our simulations is widely used in the community (see the dynamo benchmark study by Jouve et al.[36] and the review by Charbonneau[6]); however, the assumed value of the turbulent diffusivity coefficient can be different in various simulations. This value sets the diffusive timescale and determines whether flux transport dynamics is dominated by diffusion or advection by meridional flow[17]. In this section, we test the robustness of our results to changes in those aspects of our model setup which are not well constrained.

We first study the impact of varying the meridional flow continuously between the old and the new random value (as opposed to the instantaneous change in our reference solutions). As outlined in Tables 1–2, the correlations between cycle overlap, polar field strength and meridional flow variations remain very similar (both qualitatively and quantitatively) to that obtained earlier in

Simulation	Ovrlp. vs. V_n		Ovrlp. vs. V_{n-1}		Ovrlp. vs. ΔV_{n-1}	
	r	p	r	p	r	p
Northern Hemisphere						
1. Reference Solution	-0.13	93.42%	-0.81	99.99%	0.45	99.99%
2. Continuous Flow Variations	-0.13	94.28%	-0.80	99.99%	0.47	99.99%
3. High Diffusivity	-0.17	97.00%	-0.38	99.99%	0.15	93.46%
4. Low Buoyant Threshold (1KG)	-0.20	99.75%	-0.63	99.99%	0.30	99.99%
Southern Hemisphere						
1. Reference Solution	-0.13	94.53%	-0.80	99.99%	0.45	99.99%
2. Continuous Flow Variations	-0.13	94.32%	-0.79	99.99%	0.46	99.99%
3. High Diffusivity	-0.17	96.61%	-0.38	99.99%	0.15	93.66%
4. Low Buoyant Threshold (1KG)	-0.19	99.65%	-0.64	99.99%	0.31	99.99%

Table 1: Correlations for overlap versus meridional flow. (1) The reference solution uses all the parameters mentioned above and is the one reported in the main manuscript. (2) In this simulation the flow no longer changes abruptly but undergoes a continuous change from one value to the other through a ramp function. The slope is set such that the largest change (15 m/s) takes three years. (3) Solution in which the supergranular diffusivity is changed from $\eta_{sg} = 10^{12}$ cm^2/s to $\eta_{sg} = 5 \times 10^{12}$ cm^2/s. (4) Simulation in which the buoyant threshold is 1 kilo-Gauss (KG).

Simulation	Br vs. V_n		Br vs. V_{n-1}		Br vs. ΔV_{n-1}	
	r	p	r	p	r	p
Northern Hemisphere						
1. Reference Solution	0.45	99.99%	-0.83	99.99%	0.87	99.99%
2. Continuous Flow Variations	0.40	99.99%	-0.82	99.99%	0.91	99.99%
3. High Diffusivity Solution	0.39	99.99%	-0.68	99.99%	0.76	99.99%
4. Low Buoyant Threshold (1KG)	0.43	99.99%	-0.74	99.99%	0.78	99.99%
Southern Hemisphere						
1. Reference Solution	0.45	99.99%	-0.83	99.99%	0.87	99.99%
2. Continuous Flow Variations	0.40	99.99%	-0.81	99.99%	0.91	99.99%
3. High Diffusivity Solution	0.38	99.99%	-0.68	99.99%	0.75	99.99%
4. Low Buoyant Threshold (1KG)	0.43	99.99%	-0.74	99.99%	0.78	99.99%

Table 2: Correlations for polar field strength versus meridional flow. (1) The reference solution uses all the parameters mentioned above and is the one reported in the main manuscript. (2) In this simulation the flow no longer changes abruptly but undergoes a continuous change from one value to the other through a ramp function. The slope is set such that the largest change (15 m/s) takes three years. (3) Solution in which the supergranular diffusivity is changed from $\eta_{sg} = 10^{12}$ cm^2/s to $\eta_{sg} = 5 \times 10^{12}$ cm^2/s. (4) Simulation in which the buoyant threshold is 1 kilo-Gauss (KG).

our reference solution. In fact, in certain cases the correlations become stronger on incorporating smoothly varying meridional flows.

Furthermore, we explore the influence of a higher turbulent diffusion coefficient with a new model run, keeping other ingredients the same as in the reference solution. With a diffusivity coefficient five times that of the reference solution in the upper part of the convection zone (which increases the role of diffusive flux transport in this region) we find that the results remain qualitatively similar, although quantitatively somewhat different. The flow speed in the early half of the cycle (v_{n-1}) still has the maximum impact on the number of spotless days (conversely, cycle overlap), although the strength of the correlation is weaker relative to the reference solution. This is expected as in these model runs, diffusive flux dispersal shares the responsibility of magnetic flux transport along with meridional circulation thereby somewhat reducing the correlation between flow speed and cycle overlap. Additionally, we find that the correlation between the polar field strength and meridional flow speed in these high diffusivity solutions is essentially similar to that of the reference solution.

Note that the toroidal and poloidal field strength are determined by the threshold for magnetic buoyancy in these kinematic simulations. In the reference solution we have set $B_c = 5 \times 10^4$ Gauss based on results of thin-flux-tube-simulations. The peak polar (radial) field strength generated in this simulation is 16.66×10^3 Gauss (9.62×10^3 Gauss for the high-diffusivity solution with the same B_c). However, full-MHD simulations can self-consistently generate toroidal field strength only on the order of 1000 Gauss[37]. We have performed additional runs with a new buoyancy

Simulation	Br vs. Ovrlp.	
	r	p
Northern Hemisphere		
1. Reference Solution	0.46	99.99%
2. Continuous Flow Variations	0.54	99.99%
3. High Diffusivity	0.10	80.02%
4. Low Buoyant Threshold (1KG)	0.32	99.99%
Southern Hemisphere		
1. Reference Solution	0.47	99.99%
2. Continuous Flow Variations	0.52	99.99%
3. High Diffusivity	0.12	85.44%
4. Low Buoyant Threshold (1KG)	0.33	99.99%

Table 3: Correlations for polar field strength versus overlap. (1) The reference solution uses all the parameters mentioned above and is the one reported in the main manuscript. (2) In this simulation the flow no longer changes abruptly but undergoes a continuous change from one value to the other through a ramp function. The slope is set such that the largest change (15 m/s) takes three years. (3) Solution in which the supergranular diffusivity is changed from $\eta_{sg} = 10^{12}$ cm^2/s to $\eta_{sg} = 5 \times 10^{12}$ cm^2/s. (4) Simulation in which the buoyant threshold is 1 kilo-Gauss (KG).

threshold of $B_c = 1000$ Gauss (i.e., 1 kilo-Gauss) to explore the consequences of making the kinematically simulated toroidal field amplitude on the same order as that in full-MHD simulations. As indicated in the accompanying tables, the relationship between the nature of solar minima and flow speed variations remain the same qualitatively as in the reference solution. We also find that in this case, the peak polar field strength reduces to 147 Gauss. Although low-resolution magnetograms which measure the (plausibly unresolved) diffuse component of the magnetic field indicate that the average field strength is on the order of tens of Gauss, recent high resolution observations from the Hinode space mission shows the existence of strong kilo-Gauss unipolar (radial) flux tubes in the polar region[38,39]. Although, it is not clear whether in reality the strong kilo-Gauss flux tubes or the much weaker (diffuse) polar field is involved in the regeneration of the toroidal field, our numerous model runs show that this is a matter of scaling; the underlying qualitative relationship between the characteristics of solar minima and flow variations remain similar.

Finally, we explore the correlation between cycle overlap and polar field strength (Table 3). We find that in the simulation using continuously varying meridional flows, the correlation is actually stronger in comparison to the reference solution. In the high diffusion case the correlation between cycle overlap and polar field strength is almost negligible; interestingly, however, a similar trend to the reference solution is still apparent (Figure 3); cycles with a large number of spotless days (high negative overlap) have consistently weaker polar field strength.

In summary therefore, we find that the main model results related to the origin of very deep

solar minima is robust with respect to reasonable changes in the simulation setup and assumptions.

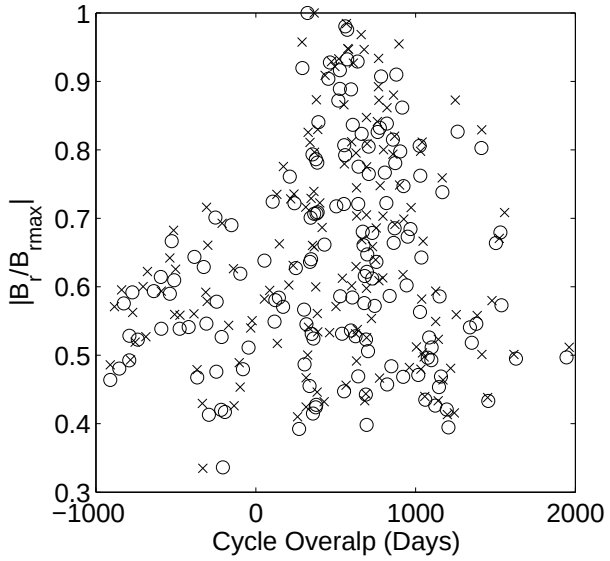

s

Figure 3: Simulated normalized polar field strength versus cycle overlap at sunspot cycle minimum in units of days for a run with supergranular diffusivity of 5×10^{12} cm^2/s. Here, $B_{max} = 9.62 \times 10^3$ Gauss.The results show that even in a high-diffusivity solution, a deep solar minimum with a large number of spotless days is typically associated with relatively weak polar field strength as indicated by the reference simulation. Crosses (circles) correspond to data from the Northern (Southern) solar hemisphere

10 A Note on Flow Observations

How do our simulations compare to observations related to the minimum of cycle 23? Helioseismic measurements of the equatorward migration of the solar internal torsional oscillation show that the

torsional oscillation pattern of the upcoming cycle 24 (which originated near the maximum of the preceding cycle) is migrating relatively slowly compared to that of cycle 23[40]. Since the torsional oscillation pattern is believed to be associated with the migration of the magnetic cycle[27], this could be indirect evidence that the meridional flow driving (the toroidal field belt of) cycle 24 in the solar interior is relatively slow compared to that of the previous cycle; this is in agreement with our theoretical simulations.

On the other hand, direct surface observations[41] indicate that the flow near the surface may have increased (roughly in a sinusoidal fashion) from the maximum of cycle 23 to its minimum – in apparent conflict with the earlier, indirect evidence of a slower flow and our simulations. However, helioseismic measurements indicate that these near-surface flow variations reduce with depth and is almost non-existent at depths of 0.979 $R_\odot$[42]. Therefore we argue that these surface variations may have no significant impact on the magnetic field dynamics in the solar interior, which is reflected in their inadequacy in reproducing the very low polar field strength at the minimum of cycle 23[28]. In support of our argument, we plot in Figure 4 the depth-dependence of the cumulative poleward mass flux amplitude in the meridional flow (based on a standard meridional flow profile) and find that only about 2% of the poleward mass-flux is contained within the surface and a depth of 0.975 $R_\odot$. Evidently, much of the flux transport dynamics associated with meridional flow occur deeper down in the solar interior – as yet inaccessible to observations – probing which is possible using dynamo simulations such as that outlined here.

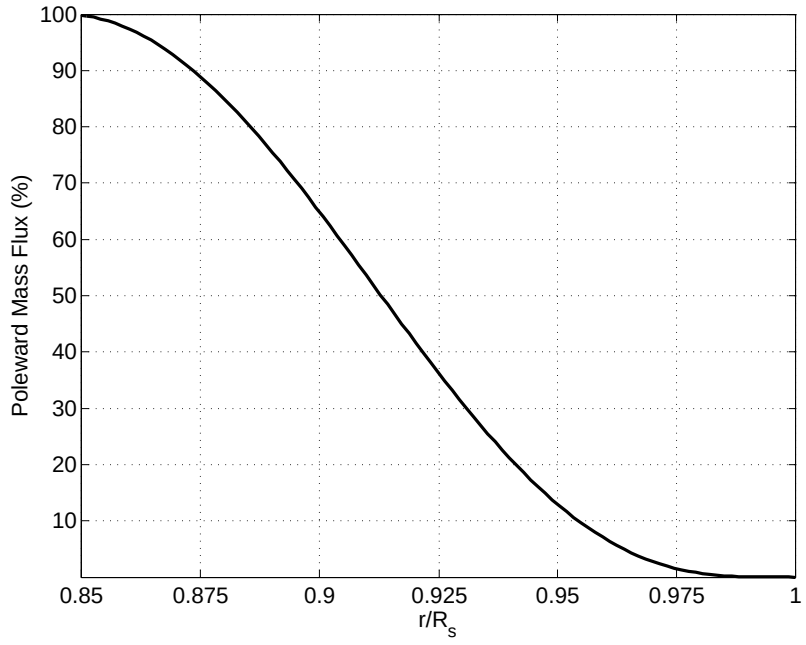

Figure 4: A plot of the cumulative meridional flow mass flux amplitude (between the radius in question and the surface; y-axis) versus depth (measured in terms of fractional solar radius $r/R_{\odot}$; x-axis). The mass flux is determined from the typical theoretical profile of meridional circulation used in solar dynamo simulations including the one described here. This estimate indicates that only about 2% of the poleward mass-flux is contained between the solar surface and a radius of 0.975 $R_{\odot}$, a region in which current (well-constrained) observations of the meridional flow is limited to.

References

29. Dasi-Espuig, M., Solanki, S. K., Krivova, N. A., Cameron, R. H. & Peñuela, T. Sunspot group tilt angles and the strength of the solar cycle. *ArXiv e-prints* (2010). 1005.1774.

30. Longcope, D. & Choudhuri, A. R. The Orientational Relaxation of Bipolar Active Regions. *Sol. Phys.* **205**, 63–92 (2002).

31. Fan, Y., Fisher, G. H. & McClymont, A. N. Dynamics of emerging active region flux loops. *Astrophys. J.* **436**, 907–928 (1994).

32. Charbonneau, P. *et al.* Helioseismic Constraints on the Structure of the Solar Tachocline. *Astrophys. J.* **527**, 445–460 (1999).

33. Hochbruck, M. & Lubich, C. On Krylov subspace approximations to the matrix exponential operator. *SIAM Journal on Numerical Analysis* **34**, 1911–1925 (1997).

34. Hochbruck, M., Lubich, C. & Selhofer, H. Exponential integrators for large systems of differential equations. *SIAM Journal on Scientific Computing* **19**, 1552–1574 (1998).

35. Christensen-Dalsgaard, J. *et al.* The Current State of Solar Modeling. *Science* **272**, 1286–+ (1996).

36. Jouve, L. *et al.* A solar mean field dynamo benchmark. *Astron. Astrophys.* **483**, 949–960 (2008).

37. Ghizaru, M., Charbonneau, P. & Smolarkiewicz, P. K. Magnetic Cycles in Global Large-eddy Simulations of Solar Convection. *Astrophys. J.* **715**, L133–L137 (2010).

38. Tsuneta, S. *et al.* The Magnetic Landscape of the Sun's Polar Region. *Astrophys. J.* **688**, 1374–1381 (2008). 0807.4631.

39. Ito, H., Tsuneta, S., Shiota, D., Tokumaru, M. & Fujiki, K. Is the Polar Region Different from the Quiet Region of the Sun? *Astrophys. J.* **719**, 131–142 (2010). 1005.3667.

40. Howe, R. *et al.* A Note on the Torsional Oscillation at Solar Minimum. *Astrophys. J.* **701**, L87–L90 (2009). 0907.2965.

41. Hathaway, D. H. & Rightmire, L. Variations in the Sun's Meridional Flow over a Solar Cycle. *Science* **327**, 1350– (2010).

42. González Hernández, I., Howe, R., Komm, R. & Hill, F. Meridional Circulation During the Extended Solar Minimum: Another Component of the Torsional Oscillation? *Astrophys. J.* **713**, L16–L20 (2010). 1003.1685.